

AD \_\_\_\_\_

Award Number: W81XWH-04-1-0042

TITLE: Transurethral Ultrasound Diffraction Tomography

PRINCIPAL INVESTIGATOR: Matthias C. Schabel, Ph.D.  
Dilip Ghosh Roy, Ph.D.  
Altaf Khan, M.S.

CONTRACTING ORGANIZATION: University of Utah  
Salt Lake City, UT 84108

REPORT DATE: March 2005

TYPE OF REPORT: Annual

PREPARED FOR: U.S. Army Medical Research and Materiel Command  
Fort Detrick, Maryland 21702-5012

DISTRIBUTION STATEMENT:

× Approved for public release; distribution unlimited

The views, opinions and/or findings contained in this report are those of the author(s) and should not be construed as an official Department of the Army position, policy or decision unless so designated by other documentation.

20060503116

**REPORT DOCUMENTATION PAGE**Form Approved  
OMB No. 074-0188

Public reporting burden for this collection of information is estimated to average 1 hour per response, including the time for reviewing instructions, searching existing data sources, gathering and maintaining the data needed, and completing and reviewing this collection of information. Send comments regarding this burden estimate or any other aspect of this collection of information, including suggestions for reducing this burden to Washington Headquarters Services, Directorate for Information Operations and Reports, 1215 Jefferson Davis Highway, Suite 1204, Arlington, VA 22202-4302, and to the Office of Management and Budget, Paperwork Reduction Project (0704-0188), Washington, DC 20503

<b>1. Agency Use Only (Leave blank)</b>		<b>2. Report Date</b> March 31, 2005	<b>3. Report Type and Period Covered (i.e., annual 1 Jun 00 - 31 May 01)</b> Annual : March 1, 2004 - February 28, 2005	
<b>4. Title and Subtitle</b> Transurethral Ultrasound Diffraction Tomography			<b>5. Award Number</b> W81XWH-04-1-0042	
<b>6. Author(s)</b> Matthias C. Schabel, Ph.D. Dilip Ghosh Roy, Ph.D. Altaf Khan, M.S.				
<b>7. Performing Organization Name (Include Name, City, State, Zip Code and Email for Principal Investigator)</b> University of Utah Salt Lake City, UT 84108  E-Mail: matthias.schabel@hsc.utah.edu			<b>8. Performing Organization Report Number (Leave Blank)</b>	
<b>9. Sponsoring/Monitoring Agency Name and Address</b>  U.S. Army Medical Research and Materiel Command Fort Detrick, Maryland 21702-5012			<b>10. Sponsoring/Monitoring Agency Report Number (Leave Blank)</b>	
<b>11. Supplementary Notes (i.e., report contains color photos, report contains appendix in non-print form, etc.)</b>				
<b>12a. Distribution/Availability Statement (check one)</b> × Approved for public release; distribution unlimited			<b>12b. Distribution Code</b>	
<b>13. Abstract (Maximum 200 Words)</b> The potential for cost-effective tomographic imaging using ultrasound continues to be confronted with difficulties arising from the computational complexity of fully three-dimensional object reconstruction in the diffraction regime. Development of fast and accurate forward and inverse models for ultrasound propagation in the biomedical frequency range of 1-10 MHz is essential for diffraction tomography to be a practical imaging modality. We have implemented a flexible, object-oriented simulation system in MATLAB for performing rapid two- and three-dimensional modeling of forward scattering using the conjugate gradient FFT method in conjunction with a fast linear adjoint approximation to the Jacobian. This system can simulate arbitrary object geometries, and is capable of performing a full forward scattering calculation for 2D objects of up to 512x512 pixels or 3D objects up to 64x64x64 voxels in size in a few minutes on a desktop computer. The accuracy of the method has been verified in the weak scattering limit with Born approximation solutions for an infinite cylinder (2D) and a sphere (3D) and over the full range of wavelengths for exact solutions in the same geometries. A nonlinear conjugate gradient inversion algorithm has been implemented and tested in both 2D and 3D, demonstrating the feasibility of the method for diffraction tomography.				
<b>14. Subject Terms (keywords previously assigned to proposal abstract or terms which apply to this award)</b> acoustic inverse scattering, acoustic tomography, Lippmann-Schwinger Equation, conjugate gradient FFT, prostate imaging			<b>15. Number of Pages</b> 34	
			<b>16. Price Code</b>	
<b>17. Security Classification of Report</b> Unclassified	<b>18. Security Classification of this Page</b> Unclassified	<b>19. Security Classification of Abstract</b> Unclassified	<b>20. Limitation of Abstract</b> Unlimited	

## Table of Contents

Cover.....	
SF 298.....	
Table of Contents.....	1
Introduction.....	2
2 Theoretical Foundation.....	3
2.1 The Helmholtz Problem . . . . .	3
2.2 Discretization of the Lippmann-Schwinger Forward Problem . . . . .	4
2.2.1 Evaluation of the 3D Green's Function Matrix . . . . .	5
2.3 Solution of the Lippmann-Schwinger Equation using the CGFFT Method . . . . .	7
2.4 Analytical Solutions in 2D and 3D . . . . .	9
2.4.1 Scattering From an Infinite, Homogeneous Circular Cylinder . . . . .	9
2.4.2 Scattering From a Homogeneous Sphere . . . . .	10
2.5 Solution of the Inverse Scattering Problem . . . . .	11
3 Numerical Results.....	14
3.1 Comparison with Born Approximation and Exact Results . . . . .	14
3.2 Performance Profiling . . . . .	15
Key Research Accomplishments.....	16
Reportable Outcomes.....	16
Conclusions.....	17
References.....	11
Appendices.....	21

# 1 Introduction

The main objective of this project is the development of accurate physical models and efficient numerical algorithms suitable for diffraction tomographic reconstruction of the compressibility, acoustic attenuation, and mass density of the prostate through a multielement transurethral ultrasound transceiver. Unlike conventional ultrasound imaging, which is non-quantitative and affected by speckle artifacts, three-dimensional tomographic solution of the inverse acoustic scattering problem has the potential to quantitatively reconstruct the detailed acoustic properties of the prostate from measurements of the scattered radiation field. However, numerous challenges must be confronted before such a proposition becomes feasible in real-world applications. It is well-known that problems in inverse scattering, in addition to being mathematically complex and computationally intensive, are also particularly ill-posed and ill-conditioned.[1, 2]

In the weak scattering limit, such problems are tractable within the so-called Born approximation, in which the pressure field internal to the scatterer is approximated by the pressure field of the incident wave. This approximation assumes negligible loss of the incident field energy through scattering, which is effectively the single scattering limit where  $\gamma \rightarrow 0$ , and  $\lambda/L \gg 1$ . The Born approximation is clearly inappropriate for imaging an object such as the prostate which may not be a weak scatterer at all, and for which multiple scattering must be taken into account. For this reason, we have taken an approach involving solution of the full multiple-scattering form of the nonuniform wave equation:

$$\nabla^2 p - \frac{1}{c^2} \frac{\partial^2 p}{\partial t^2} = \frac{1}{c^2} \frac{\partial^2 p}{\partial t^2} \gamma_\kappa(\mathbf{r}, t) + \nabla \cdot (\gamma_\rho(\mathbf{r}, t) \nabla p) - 2 \nabla \cdot \mathfrak{R} \cdot \nabla, \quad (1)$$

recast in the form of a Lippmann-Schwinger integral equation:

$$p_\omega(\mathbf{r}) = p_{inc}(\mathbf{r}) + \int_{\Omega} (k^2 \gamma_\kappa p_\omega G_\omega(\mathbf{r}|\mathbf{r}_0) + \gamma_\rho \nabla_0 p_\omega \cdot \nabla_0 G_\omega(\mathbf{r}|\mathbf{r}_0)) d\mathbf{r}_0, \quad (2)$$

as discussed in Morse and Ingard.[3] Our initial implementation has only considered variations in compressibility in the scatterer, neglecting the second term in Eq. 2; incorporation of density inhomogeneities in the forward model will constitute a significant component of work in the upcoming year.

The characteristic physical scales of the problem are:  $L \sim 5$  cm,  $c \sim 2.5 \times 10^5$  cm/s,  $\nu \sim 1 - 5 \times 10^6$  s<sup>-1</sup>,  $\lambda \sim 0.05 - 0.25$  cm. Given that

cell sizes must be on the order of  $\lambda/4$ , for a realistic geometry we expect grid dimensions of  $\sim 100 - 500$  pixels in each dimension, corresponding to  $N_p \sim 10^4 - 2.5 \times 10^5$  in 2D and  $N_p \sim 10^6 - 1.25 \times 10^8$  in 3D. Furthermore, iterative nonlinear inversion methods may require many evaluations of the forward model to reach convergence. For these reasons, development of highly efficient methods for computation of the forward model is critical to the success of the proposed work. A significant component of the work described in the following report has centered on theoretical analysis of the scattering equation and computational implementation and validation of the forward model in both 2D and 3D. Our model is capable of solving the full scattering problem on a desktop computer (2 GHz PowerMac G5) on a  $1024 \times 1024$  grid in 2D (see Fig. 1) or a  $100 \times 100 \times 100$  grid in 3D in approximately 30 minutes of runtime, and has been structured in a way that is highly amenable to parallelization in anticipation of work to be done in the upcoming months.

## 2 Theoretical Foundation

### 2.1 The Helmholtz Problem

We begin by briefly reviewing the basic Helmholtz problem:

$$(\Delta + \kappa_0^2 n(\mathbf{x})) \psi(\mathbf{x}) = 0 \text{ where } \mathbf{x} \in \mathbb{R}^d : d \in \{2, 3\}, \quad (3)$$

where the following limit holds uniformly in all directions:

$$\lim_{|\mathbf{x}| \rightarrow \infty} \left( |\mathbf{x}|^{1-d} \psi'(\mathbf{x}) - ik_0 \right) = 0, \quad (4)$$

Here,  $\psi(\mathbf{x})$  represents the total pressure field.  $n(\mathbf{x})$  is the refractive index is defined by  $n(x) = c_0^2/c^2(\mathbf{x})$ , where  $c_0$  and  $c(\mathbf{x})$  are sound velocities in the ambient medium and the object, respectively. A typical scattering geometry is shown in Fig. 2.

In the case of scattering by inhomogeneities, it is customary to express the Helmholtz problem in terms of the of relative change in the refractive index. Therefore, we define a quantity  $\gamma(\mathbf{x}) = 1 - n(\mathbf{x}) = 1 - \kappa_0/\kappa(\mathbf{x})$ , where  $\kappa$  is the compressibility. With this definition, and a homogeneous background medium, we observe that  $\gamma(\mathbf{x})$  has compact support on the inhomogeneous scatterer which is to be recovered. In a non-attenuating medium,  $\gamma(\mathbf{x})$  is a

pure real number, while an attenuating medium has a complex value:  $\gamma(\mathbf{x}) = \gamma_r(\mathbf{x}) + i\gamma_i(\mathbf{x})$

The formal solution of the Helmholtz problem may be expressed as a Lippmann-Schwinger integral equation:

$$\psi(\mathbf{x}) = \psi^{inc}(\mathbf{x}) - k_0^2 \int_{\Omega} d\mathbf{x}' G^{(0)}(k_0|\mathbf{x} - \mathbf{x}'|) \gamma(\mathbf{x}') \psi(\mathbf{x}'), \quad (5)$$

where  $\Omega \in \mathbb{R}^d$  is a volume bounding the scattering object.[1, 2] The incident scattered wave is represented by a plane wave:  $\psi^{inc}(\mathbf{x}) = e^{i\mathbf{k}_0 \cdot \mathbf{x}}$ , where the wavenumber  $k_0 = |\mathbf{k}_0| = 2\pi/\lambda$  and  $\lambda$  is the wavelength.  $\psi(\mathbf{x})$  represents the total field, comprised of incident and scattered components:  $\psi(\mathbf{x}) = \psi^{inc}(\mathbf{x}) + \psi^{sc}(\mathbf{x})$ .  $G^{(0)}(\mathbf{x}|\mathbf{x}_s)$  is the free space Green's function:

$$G^{(0)}(\mathbf{x}|\mathbf{x}_s) = -\frac{i}{4} H_0^1(k_0|\mathbf{x} - \mathbf{x}_s|) \quad \text{in } \mathbb{R}^2, \quad (6)$$

and

$$G^{(0)}(\mathbf{x}|\mathbf{x}_s) = \frac{1}{4\pi} |\mathbf{x} - \mathbf{x}_s|^{-1} e^{ik_0|\mathbf{x} - \mathbf{x}_s|} \quad \text{in } \mathbb{R}^3. \quad (7)$$

In all the above expressions,  $\mathbf{x}$  is the field or observation point and  $\mathbf{x}_s$  is the source location. Equation 5 is, in principle, valid for all  $\mathbf{x} \in \mathbb{R}^d$ , being applicable both within and outside  $\Omega$ . The scattered field,  $\psi^{sc}(\mathbf{x})$ , at the detector position  $\mathbf{x}_D$  can thus be obtained:

$$\psi^{sc}(\mathbf{x}_D) = -k_0^2 \int_{\Omega} d\mathbf{x}' G^{(0)}(k_0|\mathbf{x}_D - \mathbf{x}'|) \gamma(\mathbf{x}') \psi(\mathbf{x}'). \quad (8)$$

## 2.2 Discretization of the Lippmann-Schwinger Forward Problem

Discretization of the integral equation of scattering (Eq. 5) was performed on a regular square lattice, though preliminary progress toward an implementation on a hexagonal lattice, which offers the benefit of increased packing density for the interpolation of the Green's functions (discussed below), has also been made. Interpolation of the Green's function over lattice-centered circular elements was first introduced by Richmond for the 2D problem,[10] (see Fig. 3) and has been extended to spherical elements in 3D in this work. For circular or spherical regions, the Green's function can be analytically integrated to accurately approximate it over the lattice, significantly speeding

up the initial computation of the discrete Green's function matrix. the accuracy of our integration scheme has been checked against full, computationally expensive, numerical quadrature of  $G$  over the individual grid cells. In addition, the Richmond-type discretization makes the discrete forward problem Nyström-like,[11] which allows interpolating the nodal values of the solution to arbitrary points in the lattice thus essentially resulting in a continuous solution.

For simplicity, the following discussion considers the 2D case except where there is a significant difference in 3D. Given a square domain,  $\Omega$ , of side  $L$  which contains the scatterer, and  $N_p = N^d$  discrete cells, Eq. 5 can be approximated for any gridpoint,  $(x_m, y_n)$ , as:

$$\psi(x_m, y_n) = \psi^{inc}(x_m, y_n) - k_0^2 \sum_{p=1}^N \sum_{q=1}^N (\gamma\psi)(x_p, y_q) \int_{\Gamma} d\mathbf{x}' G^{(0)}(k_0|\mathbf{x} - \mathbf{x}'|), \quad (9)$$

In Eq. (3),  $a = L/N$  is the lattice spacing,  $(x_m, y_n) = a(m, n)$  is the coordinate of a single gridpoint,  $(\gamma\psi)(x_p, y_q) = \gamma(x_p, y_q)\psi(x_p, y_q)$  and the integration domain,  $\Gamma$ , is a single cell  $(x_m, y_n) \rightarrow (x_{m+1}, y_{n+1})$ . Using the Richmond approach,  $\Gamma$  is approximated as a circle of area equal to the corresponding cell in 2D:  $r_0 = (1/\pi)^{1/2} : \mathbb{R}^2$ , and as a sphere of volume equal to the corresponding cell in 3D:  $r_0 = (3/4\pi)^{1/3} : \mathbb{R}^3$ .

In two dimensions, the integral in Eq. 9 can be reduced to

$$\int_{\Gamma} d\mathbf{x}' G^{(0)}(k_0|\mathbf{x} - \mathbf{x}'|) = \begin{cases} \frac{\pi k_0 r_0}{2i} J_1(k_0 r_0) H_0^{(1)}(k_0 x) & \mathbf{x} \neq \mathbf{x}' \\ \frac{\pi k_0 r_0}{2i} H_1^{(1)}(k_0 r_0) + 1 & \mathbf{x} = \mathbf{x}' \end{cases}, \quad (10)$$

in 2D and to

$$\int_{\Gamma} d\mathbf{x}' G^{(0)}(k_0|\mathbf{x} - \mathbf{x}'|) = \begin{cases} -i(k_0 r_0)^2 j_1(k_0 r_0) h_0^{(1)}(k_0 x) & \mathbf{x} \neq \mathbf{x}' \\ 1 - e^{ik_0 r_0} (1 - ik_0 r_0) & \mathbf{x} = \mathbf{x}' \end{cases}, \quad (11)$$

in 3D, where  $J_n(z)$ ,  $H_n^{(m)}(z)$ ,  $j_n(z)$ , and  $h_n^{(m)}(z)$  are the standard cylindrical and spherical Bessel and Hankel functions.[12]

### 2.2.1 Evaluation of the 3D Green's Function Matrix

The task here is to evaluate the integral

$$\mathcal{I} = -k_0^2 \int_{\Gamma} G^{(0)}(k_0|\mathbf{x} - \mathbf{x}'|) d\mathbf{x}' \quad (12)$$

of the free space Green's function over a spherical resolution element,  $\Gamma' = \mathcal{B}(r_0)$  with radius  $r_0$ , which separates into two cases: (1)  $|\mathbf{x}| > |\mathbf{x}'|$ , and (2)  $|\mathbf{x}| = |\mathbf{x}'|$  that are considered separately below.

**Off-Diagonal Terms ( $|\mathbf{x}| > |\mathbf{x}'| : \mathbf{x} \notin \Gamma'$ ):** The multipole expansion of  $G^{(0)}$  gives

$$G^{(0)}(k_0|\mathbf{x} - \mathbf{x}'|) = ik_0 \sum_{n=0}^{\infty} \sum_{m=-n}^n \alpha_{nm} h_n^{(1)}(k_0 x) P_n^m(\sin \phi) e^{-im\theta} \cdot \quad (13)$$

$$j_n(k_0 x') P_n^m(\sin \phi') e^{-im\theta'},$$

where  $\mathbf{x} = (r, \theta, \phi)$  and  $\mathbf{x}' = (r', \theta', \phi')$  are the coordinates of the field and the source point, respectively, and  $P_n^m(\mathbf{x})$  is the associated Legendre polynomial.[12] The  $\mathbf{x}'$ -integration over the ball yields

$$\int_{\Gamma'} j_n(k_0 x') P_n^m(\sin \phi') e^{-im\theta'} d\mathbf{x}' = \frac{4\pi}{k_0^3} (\sin(k_0 r_0) - (k_0 r_0) \cos(k_0 r_0)), \quad (14)$$

using  $\int dz z^2 j_0(z) = \sin(z) - z \cos(z)$ . From Eqs. 13 and 14, the off-diagonal elements of the Green's function matrix,  $\mathcal{G}_{mn}^{(0)}$  are found to be:

$$\begin{aligned} \mathcal{G}_{mn, m \neq n}^{(0)} &= -i h_0^{(1)}(k_0 x) (\sin(k_0 r_0) - (k_0 r_0) \cos(k_0 r_0)) \\ &= -i (k_0 r_0)^2 j_1(k_0 r_0) h_0^{(1)}(k_0 x). \end{aligned} \quad (15)$$

**Diagonal Terms ( $|\mathbf{x}| = |\mathbf{x}'| : \mathbf{x} \in \Gamma'$ ):** In order to calculate the diagonal elements, it is necessary to divide a resolution element into two separate regions and consider the integration over each of the regions separately. The geometry is shown in Fig. 4. In region I, we let  $\rho = |\mathbf{x} - \ell|$ , where  $\ell$  is the center of the resolution element nearest to the field point  $\mathbf{x}$ . The calculation for this region is identical to that for the off-diagonal terms computed above, yielding:

$$\begin{aligned} -k_0^2 G^{(0)} &= -i h_0^{(1)}(k_0 \rho) (\sin(k_0 \rho) - (k_0 \rho) \cos(k_0 \rho)) \\ &= -i (k_0 \rho)^2 j_1(k_0 \rho) h_0^{(1)}(k_0 \rho). \end{aligned} \quad (16)$$

In the annular region II, the integral is similar, noting that the spherical



Hankel function may be written as  $h_0^{(1)}(z) = j_0(z) + iy_0(z)$ ,

$$\begin{aligned} -k_0^2 G_{mm}^{(0)} &= -ij_0(k_0\rho) \int_{k_0\rho}^{k_0r_0} dr r^2 h_0^{(1)}(r) \\ &= -ij_0(k_0\rho) \left( \int_{k_0\rho}^{k_0r_0} dr r^2 j_0(r) + i \int_{k_0\rho}^{k_0r_0} dr r^2 y_0(r) \right). \end{aligned} \quad (17)$$

This equation is evaluated using the integrals

$$\int dz z^2 j_0(z) = \sin(z) - z \cos(z), \quad (18)$$

and

$$\int dz z^2 y_0(z) = -(\cos(z) + z \cos(z)), \quad (19)$$

giving

$$\mathcal{G}_{mm}^{(0)} = 1 - e^{ik_0r_0} (1 - ik_0r_0). \quad (20)$$

### 2.3 Solution of the Lippmann-Schwinger Equation using the CGFFT Method

Here we discuss the conjugate gradient fast Fourier transform (CGFFT) method as applied to the solution of Eq. 9. If we attempt to solve this discretized Lippmann-Schwinger equation by direct matrix inversion, we have:

$$\psi = (I - \mathcal{G}^{(0)}\Lambda)^{-1} \psi^{inc}, \quad (21)$$

where  $\Lambda$  is a  $N_p \times N_p$  matrix having the values of  $\gamma$  along the diagonal:  $\Lambda_{ii} = \gamma_i$ . For  $\gamma$  having  $N_p = N^d$  elements, the operation count is  $\mathcal{O}(N^{3d})$ , making direct inversion impractical for any reasonable sized scatterer. However, since the summation in Eq. 9 is in fact a  $d$ -dimensional convolution it may be evaluated by fast Fourier transform (FFT) in  $\mathcal{O}(N^d \log N^d)$  operations, leading to a tremendous speedup for non-trivial grid sizes.[9] This allows us to formulate the forward model as:

$$\psi = \psi^{inc} - \mathcal{G}^{(0)} \star (\gamma\psi), \quad (22)$$

which becomes, after Fourier transformation,

$$\mathcal{F}\{\psi\} = \mathcal{F}\{\psi^{inc}\} - \mathcal{F}\{\mathcal{G}^{(0)}\} \mathcal{F}\{(\gamma\psi)\}, \quad (23)$$

so

$$\psi = \psi^{inc} - \mathcal{F}^{-1} \{ \mathcal{F} \{ \mathcal{G}^{(0)} \} \mathcal{F} \{ (\gamma\psi) \} \}. \quad (24)$$

We solve the resulting large linear system iteratively using the linear conjugate gradient approach.[4, 5, 6, 7, 8] The Lippmann-Schwinger operator is:

$$\hat{L}\psi = \psi - \mathcal{G}^{(0)} \star (\gamma\psi). \quad (25)$$

The adjoint Lippmann-Schwinger operator,  $\hat{L}^A$ , can be calculated from the Hilbert space relation:

$$\langle \hat{L}\psi, \phi \rangle = \langle \psi, \hat{L}^A\phi \rangle, \quad (26)$$

where the inner product,  $\langle \psi, \phi \rangle$  is

$$\langle \psi, \phi \rangle = \int \psi(\mathbf{x}) \phi^\dagger(\mathbf{x}) d\mathbf{x}, \quad (27)$$

$\phi^\dagger$  denoting the complex conjugate of  $\phi$ . Evaluating the inner product expression and noting that  $G^{(0)}(\mathbf{x}|\mathbf{x}') = G^{(0)}(\mathbf{x}'|\mathbf{x})$  yields the desired adjoint operator, namely

$$(\hat{L}^A\phi)(\mathbf{x}) = \phi(\mathbf{x}) - \gamma(\mathbf{x}) \int_{\Omega} G^{(0)\dagger}(k_0|\mathbf{x} - \mathbf{x}'|) \phi(\mathbf{x}') d\mathbf{x}'. \quad (28)$$

An outline of our CGFFT routine follows:

- Initial step:

$$\begin{aligned} \mathbf{R}_0 &= \mathbf{L}\psi_0 - \psi^{inc} \\ \mathbf{P}_1 &= -\mathbf{L}^A\mathbf{R}_0 \end{aligned}$$

- iterative steps (  $k=1,2,\dots$ ):

$$\alpha_k = \frac{\langle \psi^{inc}, \mathbf{L}\mathbf{P}_k \rangle}{\|\mathbf{L}\mathbf{P}_k\|^2} = \frac{\|\mathbf{L}^A\mathbf{R}_{k-1}\|^2}{\|\mathbf{L}\mathbf{P}_k\|^2}$$

$$\psi_k = \psi_{k-1} + \alpha_k \mathbf{P}_k$$

$$\mathbf{R}_k = \mathbf{L}\psi_k - \psi^{inc} = \mathbf{R}_{k-1} + \alpha_k \mathbf{L}\mathbf{P}_k$$

$$\beta_k = \frac{\|\mathbf{L}^A\mathbf{R}_k\|^2}{\|\mathbf{L}^A\mathbf{P}_{k-1}\|^2}$$

$$\mathbf{P}_{k+1} = \beta_k \mathbf{P}_k - \mathbf{L}^A\mathbf{R}_k$$

The residual norm

$$\frac{\|\mathbf{R}_k\|}{\|\psi^{inc}\|} = \frac{\|\mathbf{L}\psi_k - \psi^{inc}\|}{\|\psi^{inc}\|}$$

decreases monotonically as the algorithm progresses, and is an useful indication of the average error in the solution after  $k$  steps.

## 2.4 Analytical Solutions in 2D and 3D

In order to verify the correctness of the CGFFT solution, closed-form benchmark solutions were computed for an infinitely long, homogeneous circular cylinder of radius  $r_0$  in 2D, and for a homogeneous sphere of radius  $r_0$  in 3D.

### 2.4.1 Scattering From an Infinite, Homogeneous Circular Cylinder

In two space dimensions, the plane wave incident field can be rewritten using the Jacobi-Anger expansion:

$$\psi^{inc}(r, \theta) = \sum_{n=-\infty}^{\infty} i^n J_n(kr) \cos(n\theta). \quad (29)$$

The internal field is then given by

$$\psi^{int}(r, \theta) = \sum_{m=0}^{\infty} b_m J_m(k_0 r) \cos(m\theta), \quad (30)$$

and the scattered field is:

$$\psi^{sc}(r, \theta) = \sum_{m=0}^{\infty} a_m H_m^{(1)}(k_0 r) \cos(m\theta). \quad (31)$$

We let  $k_0$  be the wavenumber in the homogeneous medium,  $k$  be the wavenumber in the cylinder, and define the impedance as  $Z = k/k_0$ . The coefficients  $a_m$  and  $b_m$  are then obtained from the continuity of pressure and radial velocities across the surface of the disk, leading to the following expressions:

$$\begin{aligned} a_m &= f_m \left( J_m(k_0 r_0) \tilde{J}_m(kr_0) Z - J_m(kr_0) \tilde{J}_m(k_0 r_0) \right) \\ b_m &= f_m \left( J_m(k_0 r_0) \tilde{H}_m^{(1)}(k_0 r_0) - H_m^{(1)}(k_0 r_0) \tilde{J}_m(k_0 r_0) \right) \end{aligned} \quad (32)$$

where

$$f_m = \begin{cases} 1/\Delta_0 & m = 0 \\ 2i^m/\Delta_m & m \neq 0 \end{cases} \quad (33a)$$

$$\Delta_m = J_m(kr_0)\tilde{H}_m^{(1)}(k_0r_0) - H_m^{(1)}(k_0r_0)\tilde{J}_m(kr_0)Z \quad (33b)$$

$$\tilde{J}_m(z) = J_{m+1}(z) - J_{m-1}(z) \quad (33c)$$

$$\tilde{H}_m(z) = H_{m+1}(z) - H_{m-1}(z). \quad (33d)$$

Here,  $H_m^{(1)}(z) = J_m(z) + iY_m(z)$  is the first kind Hankel function,  $J_m(z)$  is the first kind Bessel function, and  $Y_m(z)$  is the second kind Bessel (or Neumann) function.

#### 2.4.2 Scattering From a Homogeneous Sphere

The 3D case closely parallels the 2D case discussed above. In three dimensions, the Jacobi-Anger expansion is:

$$\psi^{inc}(r, \phi) = \sum_{n=0}^{\infty} i^n (2n+1) j_n(kr) P_n(\sin \phi), \quad (34)$$

where the azimuthal angle,  $\phi$ , is measured with respect to the  $r\theta$ -plane. The internal field is then:

$$\psi^{int}(r, \theta) = \sum_{m=0}^{\infty} b_m j_m(k_0r) P_m(\sin \phi), \quad (35)$$

and the scattered field is:

$$\psi^{sc}(r, \phi) = \sum_{m=0}^{\infty} a_m j_m^{(1)}(k_0r) P_m(\sin \phi). \quad (36)$$

Again, the coefficients are determined by requiring continuity of pressure and radial velocity at the interface, giving:

$$\begin{aligned} a_m &= f_m (j_m(k_0r_0)\tilde{J}_m(kr_0)Z - j_m(kr_0)\tilde{J}_m(k_0r_0)) \\ b_m &= f_m (j_m(k_0r_0)\tilde{H}_m^{(1)}(k_0r_0) - h_m^{(1)}(k_0r_0)\tilde{J}_m(k_0r_0)) \end{aligned} \quad (37)$$

where

$$f_m = \begin{cases} 1/\Delta_0 & m = 0 \\ 2i^m(2m+1)/\Delta_m & m \neq 0 \end{cases} \quad (38a)$$

$$\Delta_m = j_m(kr_0)\tilde{h}_m^{(1)}(k_0r_0) - h_m^{(1)}(k_0r_0)\tilde{j}_m(kr_0)Z \quad (38b)$$

$$\tilde{j}_m(z) = \frac{1}{2m+1} ((m+1)j_{m+1}(z) - mj_{m-1}(z)) \quad (38c)$$

$$\tilde{h}_m(z) = \frac{1}{2m+1} ((m+1)h_{m+1}(z) - mh_{m-1}(z)). \quad (38d)$$

Here,  $h_m^{(1)}(z) = j_m(z) + in_m(z)$  is the first kind spherical Hankel function,  $j_m(z) = \sqrt{\pi/(2z)}J_{m+1/2}(z)$  is the first kind spherical Bessel function, and  $n_m(z) = \sqrt{\pi/(2z)}Y_{m+1/2}(z)$  is the second kind spherical Bessel (or Neumann) function.

## 2.5 Solution of the Inverse Scattering Problem

Our ultimate objective is the efficient and accurate reconstruction of the unknown object based on the measured scattered field (amplitude and/or phase) at a number of detector locations and incident frequencies. Due to the incomplete nature of the measured data and the effect of measurement noise, solution of such inverse problems relies on the use of ancillary prior information, typically incorporated as an *ad hoc* regularizing term in  $\Phi$  which mediates the delicate balance between the agreement between the simulated and measured scattered fields,  $\psi$  and  $\psi^{obs}$ , respectively, and the "reasonableness" of the reconstructed object. A general expression for the objective function is

$$\Phi(\gamma) = \Phi^{fit}(\gamma) + \alpha\Phi^0(\gamma), \quad (39)$$

where  $\mathcal{R}$  is an arbitrary regularizing functional which represents the concordance between the reconstructed object and our prior expectations and  $\alpha$  is a regularizing parameter which represents the weight assigned to our prior,  $\Phi^0$ , relative to the fit quality,  $\Phi^{fit}$ . Commonly,  $\Phi^{fit}$  is chosen to be the  $\chi^2$  statistic and  $\Phi^0$  to be the square of the object's norm:

$$\begin{aligned} \Phi(\gamma) &= \chi^2 + \alpha\|\gamma\|^2 \\ &= \frac{1}{2}(\psi - \psi^{obs})^T \Sigma^{-1}(\psi - \psi^{obs}) + \alpha\|\gamma\|^2, \end{aligned} \quad (40)$$

where  $\Sigma$  is the covariance matrix of the measured data. For discrete observations with uncorrelated noise,  $\Phi(\gamma)$  becomes:

$$\Phi(\gamma) = \sum_{m=1}^{N_{obs}} \left| \frac{\psi_m - \psi_m^{obs}}{\sigma_m} \right|^2 + \alpha \sum_{n=1}^{N_p} |\gamma_n|^2, \quad (41)$$

where  $\sigma_m$  is the standard deviation of the noise for the  $m$ -th detector. In general, the objective function is a complicated nonlinear equation which may have many local minima, the minimization of which should ideally lead to a reconstructed object as close as possible to the true object.

As pointed out in the introduction, a primary concern is the efficient computation of the functional (Frechét) derivatives,  $\nabla_\gamma \Phi$ , of the objective function,  $\Phi$ , with respect to the object to be reconstructed,  $\gamma$ . Conventionally, this gradient would be evaluated by straightforward differentiation:

$$\begin{aligned} \frac{d\Phi(\gamma)}{d\gamma_i} &= \sum_{m=1}^{N_{obs}} \left[ \left( \frac{\psi_m - \psi_m^{obs}}{\sigma_m} \right)^\dagger \frac{d\psi_m}{d\gamma_i} \frac{1}{\sigma_m} + \left( \frac{d\psi_m}{d\gamma_i} \frac{1}{\sigma_m} \right)^\dagger \left( \frac{\psi_m - \psi_m^{obs}}{\sigma_m} \right) \right] \\ &\quad + \alpha \sum_{n=1}^{N_p} \left[ \gamma_n^\dagger \frac{d\gamma_n}{d\gamma_i} + \gamma_n \left( \frac{d\gamma_n}{d\gamma_i} \right)^\dagger \right] \\ &= \sum_{m=1}^{N_{obs}} \frac{1}{\sigma_m^2} \left[ (\psi_m - \psi_m^{obs})^\dagger \mathbf{J}_{mi} + \mathbf{J}_{mi}^\dagger (\psi_m - \psi_m^{obs}) \right] \\ &\quad + \alpha \sum_{n=1}^{N_p} [\gamma_n^\dagger \delta_{ni} + \gamma_n \delta_{ni}] \\ &= \sum_{m=1}^{N_{obs}} \frac{1}{\sigma_m^2} \left[ (\psi_m - \psi_m^{obs})^\dagger \mathbf{J}_{mi} + \mathbf{J}_{mi}^\dagger (\psi_m - \psi_m^{obs}) \right] + 2\alpha \Re \{ \gamma_n \}. \end{aligned} \quad (42)$$

Obviously, evaluation of the full Jacobian matrix,  $\mathbf{J}$ , at every iteration involves significant computational expense and should be avoided. This can be accomplished by the computation of the gradient by the method of adjoint fields,[14, 15, 16] which is briefly described here. From the gradient expression above, the total variation  $\delta\Phi$  in  $\Phi$  for a variation  $\delta\gamma$  in  $\gamma$  is given by:

$$\delta\Phi = \Re \left\{ \sum_{m=1}^{N_{obs}} (\psi_m - \psi_m^{obs})^\dagger \delta\psi_m \right\}, \quad (43)$$

where the residual  $R_m$  is defined as  $\psi_m - \psi_m^{obs}$ , and  $\delta\psi_m$  is the variation in  $\psi_m$ . Now, from the Lippmann-Schwinger equation:

$$\psi = \mathcal{G}^{(0)}(x_m|x) \star (\gamma\psi)(x), \quad (44)$$

taken over the computational grid  $\Omega$ . Then

$$\delta\psi_m = \mathcal{G}^{(0)}(x_m|x) \star (\gamma\delta\psi + \psi\delta\gamma). \quad (45)$$

Substituting Eq. 45 for  $\delta\psi_m$  into Eq. 43 gives:

$$\delta\Phi = \Re \{ \phi^{(0)} \star (\gamma\delta\psi + \psi\delta\gamma) \} \quad (46)$$

$\phi^{(0)}$  in Eq. 46 is given by

$$\phi^{(0)} = \sum_{m=1}^{N_{obs}} R_m \star G^{(0)}(x_m|x) \quad (47)$$

which is a function on the computational grid. Let  $\phi^{(0)}$  be considered as the incident field in the Lippmann-Schwinger equation. Then:

$$\phi(x) = \phi^{(0)}(x) + \langle G^{(0)}, \gamma\phi \rangle, \quad (48)$$

where  $\phi$  is the total field corresponding to the incident field  $\phi^{(0)}$ . Equation 48 then solves  $\phi$  as:

$$\phi = [I - \mathcal{G}^{(0)}\Lambda_\gamma]^{-1}\psi^{(0)}. \quad (49)$$

But from the Lippmann-Schwinger equation, we also have:

$$\delta\psi = [I - \mathcal{G}^{(0)}\Lambda_\gamma]^{-1}\psi, \quad (50)$$

which leads to, after some algebra,

$$\begin{aligned} \delta\phi &= Re \int_{\Omega} dx (\phi(x)\psi(x))\delta\gamma(x) \\ &= Re \int_{\Omega} dx (\nabla\gamma\Phi)\delta\gamma(x), \end{aligned}$$

from which

$$\nabla_\gamma\Phi(x) = Re(\psi(x)\phi(x)), \quad x \in \Omega \quad (51)$$

### 3 Numerical Results

Here we compare the results of our CGFFT solutions of the Lippmann-Schwinger equation for both  $\psi^{int}(\mathbf{x})$  and  $\psi^{sc}(\mathbf{x})$  with the results of Born approximation calculations in 2D and with the corresponding exact analytical expressions derived in the previous section in both 2D and 3D. We also demonstrate simulations for scattering from a square object in 2D for various incidence angles. Finally, we present preliminary results of performance profiling and discuss the significance for the inverse problem.

#### 3.1 Comparison with Born Approximation and Exact Results

Figure 5 shows results for the absolute magnitude of the scattered field, along with the real and imaginary components, from an infinite circular cylinder in 2D for two different parameter regimes. Born approximation results are shown by the blue dots, the exact calculation by red dots, and the CGFFT computation by black circles. Plots on the left side of the figure are for a parameter regime well within the realm of applicability for the Born approximation, as is evidenced by the extremely high degree of concordance between all three computations. Where any discrepancy at all is discernible, it is the Born data which deviate slightly from the exact and CGFFT results which are essentially indistinguishable. The right half of the figure presents a much more challenging test case in a parameter regime where the Born approximation is clearly invalid. Here, the plots confirm our expectations; the Born data deviate dramatically from the exact solution. However, as before, the results of the CGFFT solution are virtually identical to the exact values for the scattered field. In Fig. 6, we show similar results for scattering into a ring of detectors oriented perpendicular to the  $r\theta$ -plane by a spherical objects. As before, the exact and CGFFT computations agree perfectly in the Born limit. In the non-Born regime, we begin to observe noticeable deviations between the exact and CGFFT solutions; however, as we have verified with numerical experimentation, these deviations stem from the necessarily much coarser discretization of the object in 3D. Despite these small discrepancies, it is clear that the CGFFT method is capturing the essential physics of scattering in the 3D case as well as in 2D.

To more accurately quantify the level of accuracy we can expect from our CGFFT algorithm, we present a comparison of  $\psi^{int}$  between CGFFT



and the exact solution for the infinite cylinder and sphere in Fig. 6. For the circle, computed on a  $512 \times 512$  lattice, we find essentially perfect agreement between the two, with a maximum discrepancy of less than 0.1 percent and an average deviation of less than 0.02 percent. Again, due to the more prominent discretization effects (both the circular and spherical objects were smoothed with a 0.5 pixel Gaussian blur filter to reduce scattering artifacts arising from pixelation at the object boundary) arising from coarser grid size in the 3D case, the error is enhanced relative to the circular object. Despite that fact, the absolute value is bounded at less than 1 percent, and averages less than 0.4 percent. In addition, the exact and CGFFT internal fields are clearly qualitatively quite similar. We demonstrate the ability to simulate more complex objects in Fig. 8, which demonstrates changes in both the internal and scattered fields with rotation of the angle of the incident radiation, as would be expected for an anisotropic object.

### 3.2 Performance Profiling

In order to assess the performance of our forward model and identify the presence of performance bottlenecks, we have investigated timing behavior in a number of cases. In Fig. 9, we present the dependence of execution time for fixed  $\gamma$  and  $\lambda$  at various lattice sizes. Plotting total execution time against  $N_p$ , the number of gridpoints, reveals behavior consistent with the  $N_p \log N_p$  expected for an algorithm which is dominated by the cost of performing forward and inverse FFTs, with a few notable discrepancies. The clear appearance of outlier data points with substantially elevated execution time is connected with FFTs on data sets which have a large prime factor; this is a well known effect in FFT optimization and emphasizes both that our algorithm is FFT-performance limited and that it is of great importance to select grid sizes with small prime factors. Another interesting outlier is the significant performance penalty associated with the  $128 \times 128$  FFT, which is 50% slower than would be expected from the performance curve. In this case, it appears that memory access collisions in the fast cache memory are causing an anomalous slowdown.

Two additional effects are observed to have a significant impact on performance, both relating to the convergence rate of the conjugate gradient algorithm and understandable as arising from progressively greater deviation from the Born approximation which is used as a starting point in our conjugate gradient algorithm. The first is seen with increasing  $\gamma$ , which cor-

responds to progressively stronger scattering from inhomogeneities with refractive properties that differ more from the background medium. Figure 10 shows a quadratic dependence on computation time with increasing values of  $\gamma$ . Similarly, in the second case of decreasing wavelength,  $\lambda$ , we expect to see increases in computation time as the spatial scale of structure in the internal field increases. Figure 11 plots the  $\lambda$ -dependence for three different 2D lattice sizes, showing consistent power law behavior, with execution time varying approximately as  $1/\lambda^{1.2}$ .

## 4 Key Research Accomplishments

- Complete theoretical analysis of problem formulation.
- Rapid adjoint computation of gradient terms validated against finite difference results.
- Implementation of efficient CGFFT algorithm for 2D and 3D forward modeling.
- Development of approximate and exact analytical solutions in 2D and 3D and validation of CGFFT algorithm against them.
- Approximate expression for Green's function validated against result of full numerical quadrature.
- Implementation of nonlinear conjugate gradient method for solution of inverse problem in 2D and 3D complete.
- Initial investigation of various forms of regularizing functional and various approaches to optimizing the convergence of minimization of the objective function.

## 5 Reportable Outcomes

- Abstract and oral presentation at the 16th Annual UCAIR Symposium, Park City UT, October 2004.

- Abstract submitted to 2005 Fully Three-Dimensional Image Reconstruction Meeting in Radiology and Nuclear Medicine, Salt Lake City UT, July 2005.
- Abstract submitted to Applied Inverse Problems 2005, Cirencester UK, July 2005.

## 6 Conclusions and Future Work

From the discussion above, it is apparent that a sufficiently accurate representation of the prostate will require a resolution for which the computational burden will exceed reasonable limits for a single processor system. Fortunately, much of the CGFFT computation is readily parallelized to take advantage of multiprocessor hardware and/or the high-performance computing cluster systems that are rapidly growing in popularity and availability. Nevertheless, while such approaches are likely to be relevant to this work, it remains critical to investigate all avenues to improving the intrinsic algorithm performance before resorting to brute force. For the upcoming year, we will work in a number of areas:

### 6.1 Improving Forward Model Performance

- preconditioning strategies for acceleration of conjugate gradient convergence
- implementation of the Non-Uniform FFT to enable the use of unevenly spaced grids
- predictor-corrector methods for minimizing evaluations of full forward model
- parallelization of forward model algorithm and testing on cluster system
- extension of theory to accommodate point source incident waves and transurethral geometry
- extension of theory and model to incorporate mass density terms and attenuation

## 6.2 The Inverse Problem

We have implemented and performed preliminary tests on the adjoint gradient inversion algorithm in both 2D and 3D, demonstrating the ability to reconstruct simple geometries in fairly low-resolution cases. However, there is much improvement to be made in the inversion algorithm. Among the strategies which we intend to employ over the next year are:

- investigation of alternative and/or hybrid minimization strategies such as simulated annealing and genetic algorithms to be used in conjunction with nonlinear conjugate gradient methods to maximize convergence rate.
- study of different regularizing functionals including total variation, maximum entropy, laplacian, and others and investigation of their impact on inverse problem convergence properties.
- analytical and numerical solution of the variational problem in 3D.
- parallelization of inversion algorithm
- development of a realistic prostate phantom using MRI and conventional ultrasound data in conjunction with anatomic information

## References

- [1] D. Colton and R. Kress: *Inverse Acoustic and Electromagnetic Scattering Theory*, Springer-Verlag, 1992.
- [2] D.N. Ghosh Roy and L. Couchman: *Inverse Problems and Inverse Scattering of Plane Waves*, Academic Press, 2002.
- [3] P.M. Morse and K.U. Ingard: *Theoretical Acoustics*, Princeton University Press, 1968.
- [4] M. Hestenes: *Conjugate Direction Methods in Optimization*, Springer-Verlag, 1980.
- [5] D.G. Luenberger: *Linear and Nonlinear Programming*, Addison-Wesley, 1984.
- [6] X.M. Xu and Q.H. Liu: Fast Spectral-Domain Method for Acoustic Scattering Problems, IEEE Trans. Ultrasonics, Ferroelectrics, and Frequency Control, vol. 48, pp. 522-529, 2001.
- [7] T.J. Peters and J.L. Volakis: Application of a conjugate gradient FFT method to scattering from thin planar material plates, IEEE Trans. Antenna Propag., vol. AP-36, pp. 518-526, 1988.
- [8] M.F. C  tedra, J.G. Cuevas and L. Nu  o: A scheme to analyze conducting plates of resonant size using the conjugate gradient method and the fast Fourier transform, IEEE Trans. Antenna Propag., vol. AP-36, pp. 1744-1752, 1988.
- [9] E.O. Brigham: *The Fast Fourier Transform*, Prentice-Hall, 1974.
- [10] J.H. Richmond: Scattering by a dielectric cylinder of arbitrary cross section shape, IEEE Trans. Antenna Propag., vol. AP-13, pp. 334-341, 1965.
- [11] K.E. Atkinson: *The Numerical Solution of the Integral Equations of the Second Kind*, Cambridge University Press, Cambridge, 1997.
- [12] M. Abramowitz and I.A. Stegun: *Handbook of Mathematical Functions*, Dover, 1972.

- [13] A.F. Peterson and R. Mittra: Method of conjugate gradient for the numerical solution of large-body electromagnetic scattering problems, J. Opt. Soc. Amer. A, vol. 2, pp. 971-977, 1985.
- [14] J.R. Bowler and S.A. Jenkins: Eddy-current impedance due to a volumetric flaw, J. Appl. Phys., vol. 70, pp. 1107-1114, 1991.
- [15] S.J. Norton: Iterative inverse scattering algorithms: Methods of computing Fréchet derivatives, JASA, vol. 106, pp. 2653-2660, 1999.
- [16] J. Wiskin: *Geometric and Integral Equation Methods for Scattering in Layered Media*, Doctoral Dissertation, Department of Mathematics, University of Utah, Salt Lake City, 1991.

## Figures

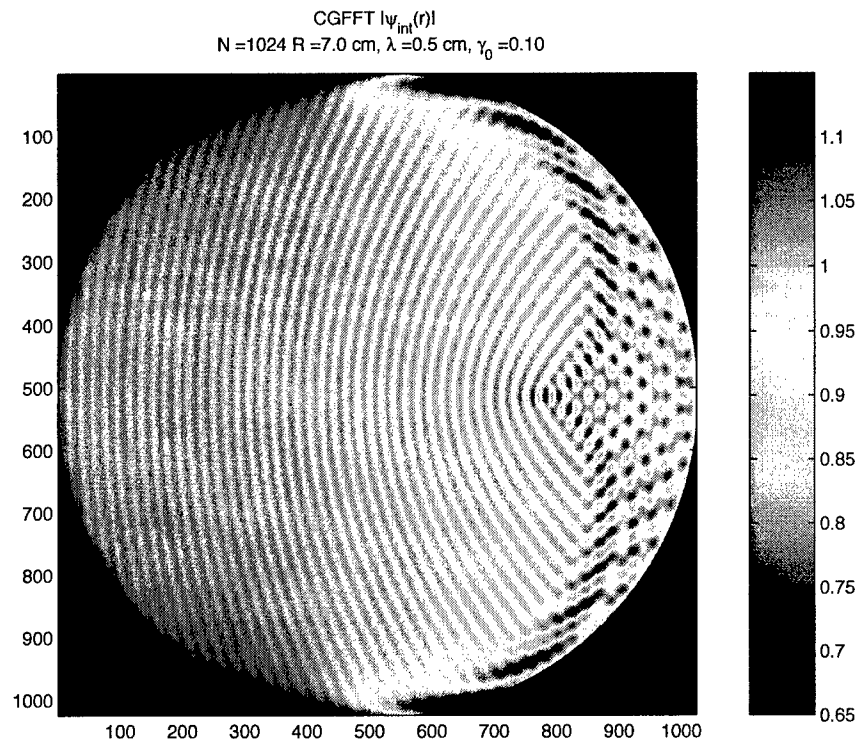


Figure 1: Internal field amplitude computed for a  $1024 \times 1024$  circular scatterer object with  $\gamma = 0.1$  and  $\lambda/L = 1/28$  for a single plane wave incident along the  $x$ -axis.



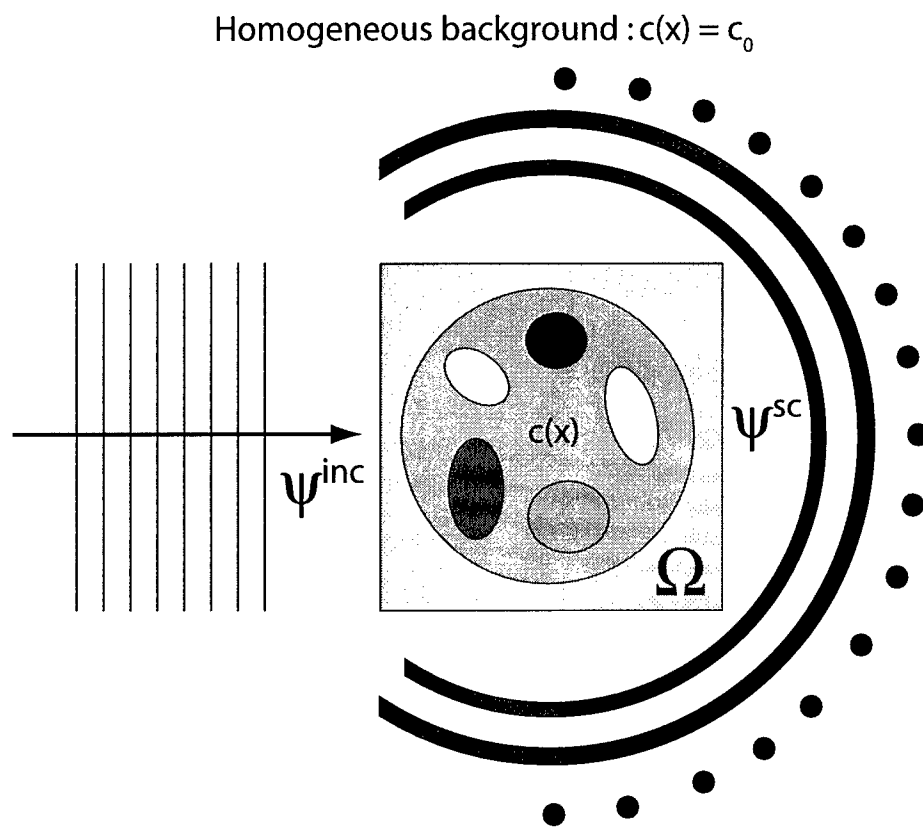


Figure 2: Schematic illustration of typical geometry of an inhomogeneity scattering problem. An incident plane wave traveling along the  $x$ -axis impinges on an object embedded in the homogeneous background medium, which is bounded by the problem domain,  $\Omega$ . Outgoing scattered waves travel in all directions from the object, and are measured at detector positions arrayed outside  $\Omega$ .

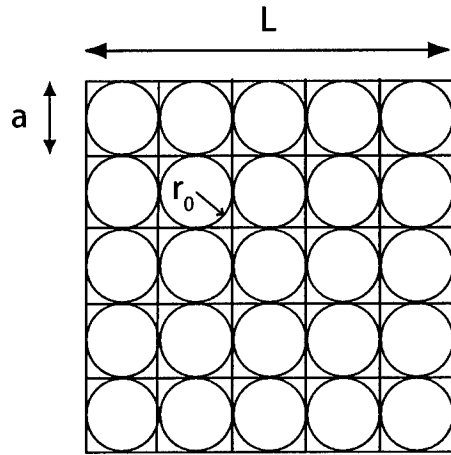


Figure 3: Schematic illustration of the discrete square lattice in 2D. The circle (extended to a sphere in 3D) of radius  $r_0$ , represents the region over which  $\gamma$  is considered homogeneous and the Green's function is analytically integrated. The radius shown is smaller than the actual radius for clarity; the actual value of  $r_0$  corresponds to an area-preserving integration.  $L$  is the physical size of the domain,  $\Omega$ , with a lattice spacing of  $a = L/N$ . Element centers are nodes for the basis functions in a Galerkin-type projection.

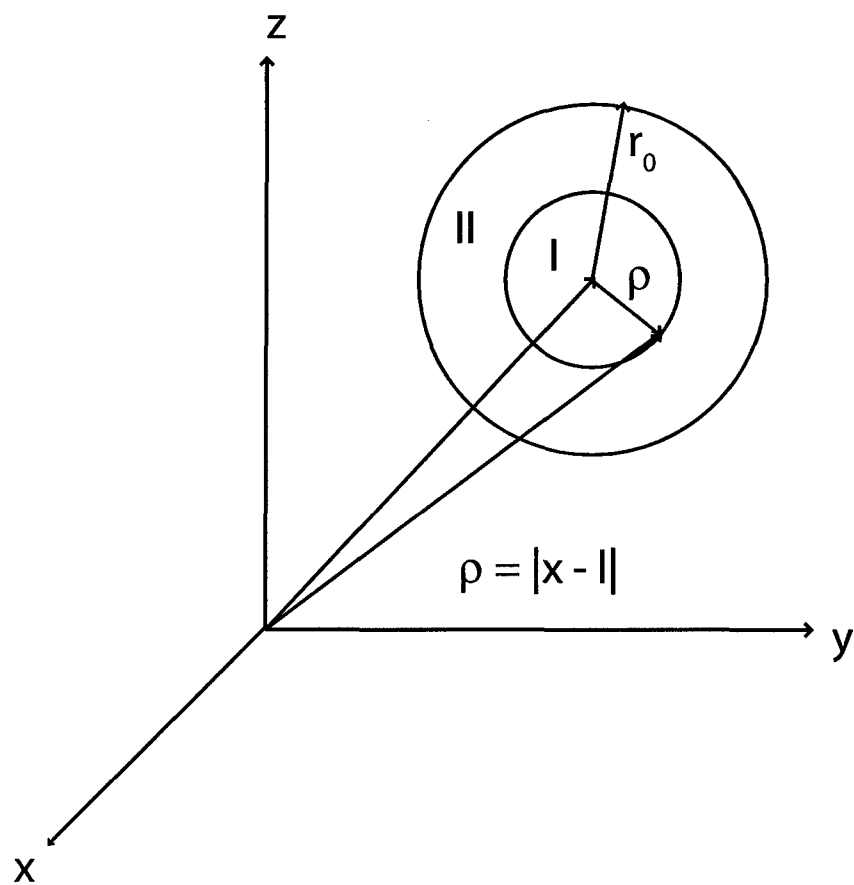


Figure 4: Illustration of the geometry used in calculating the diagonal elements of the Green's function matrix.

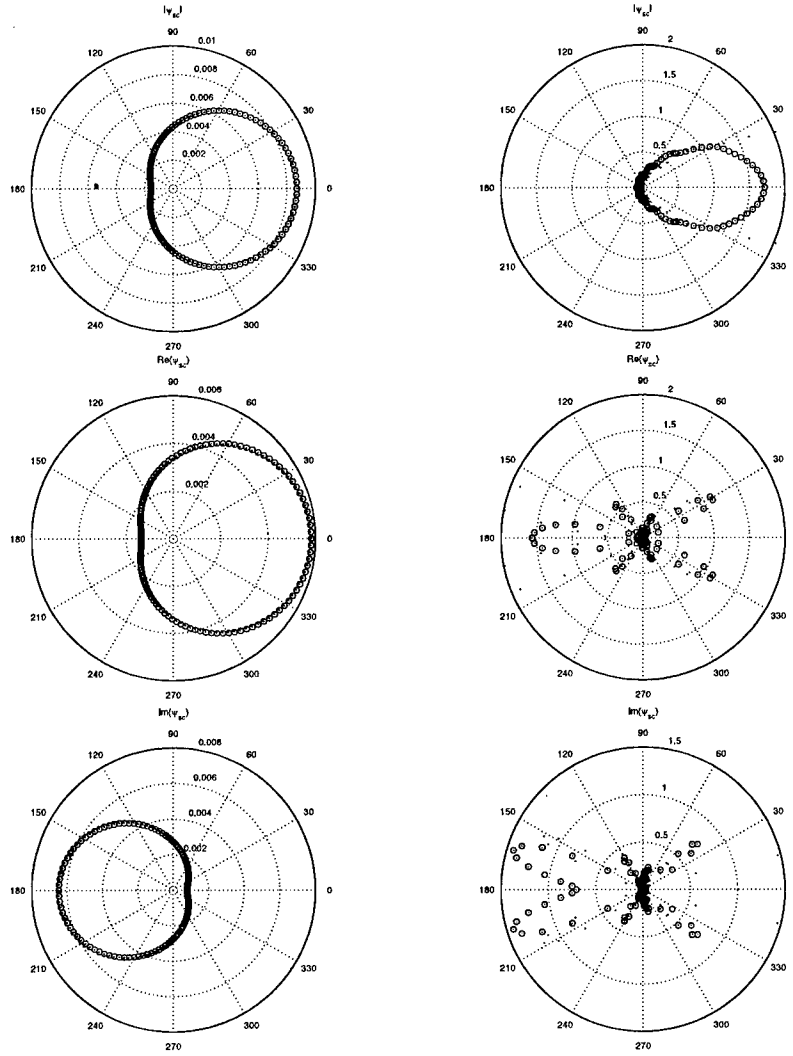


Figure 5: Comparison of  $\psi_{sc}$  for CGFFT (black circles), exact solution (red dots), and the Born approximation (blue dots) for scattering from an infinite cylinder, represented on a  $128 \times 128$  grid. The upper panels plot  $|\psi_{sc}|$ , the middle plot  $\Re\{\psi_{sc}\}$ , and the bottom panels plot  $\Im\{\psi_{sc}\}$ . Panels on the left are for  $L = 14$  cm,  $\lambda = 28$  cm, and  $\gamma = 0.01$ , while panels on the right are for  $L = 14$  cm,  $\lambda = 3.5$  cm, and  $\gamma = 0.3$ .

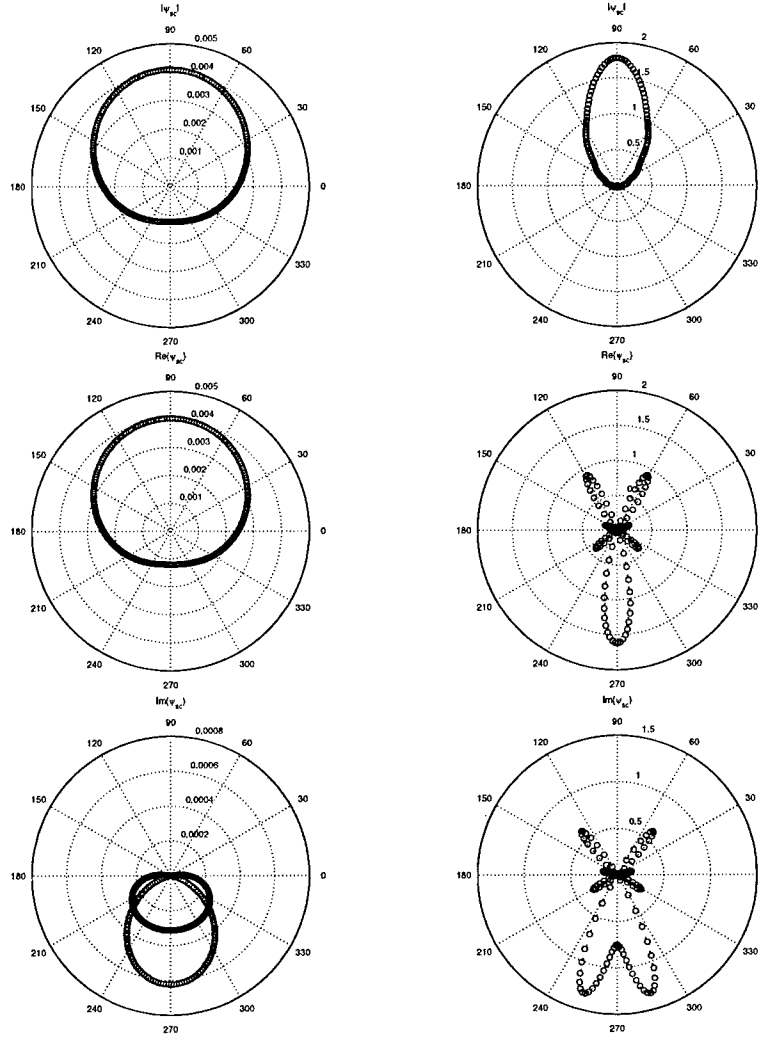


Figure 6: Comparison of  $\psi_{sc}$  for CGFFT (black circles), exact solution (red dots), and the Born approximation (blue dots) for scattering from a sphere, represented on a  $32 \times 32 \times 32$  grid. The upper panels plot  $|\psi_{sc}|$ , the middle plot  $\Re\{\psi_{sc}\}$ , and the bottom panels plot  $\Im\{\psi_{sc}\}$ . Panels on the left are for  $L = 14$  cm,  $\lambda = 28$  cm, and  $\gamma = 0.01$ , while panels on the right are for  $L = 14$  cm,  $\lambda = 3.5$  cm, and  $\gamma = 0.3$ .

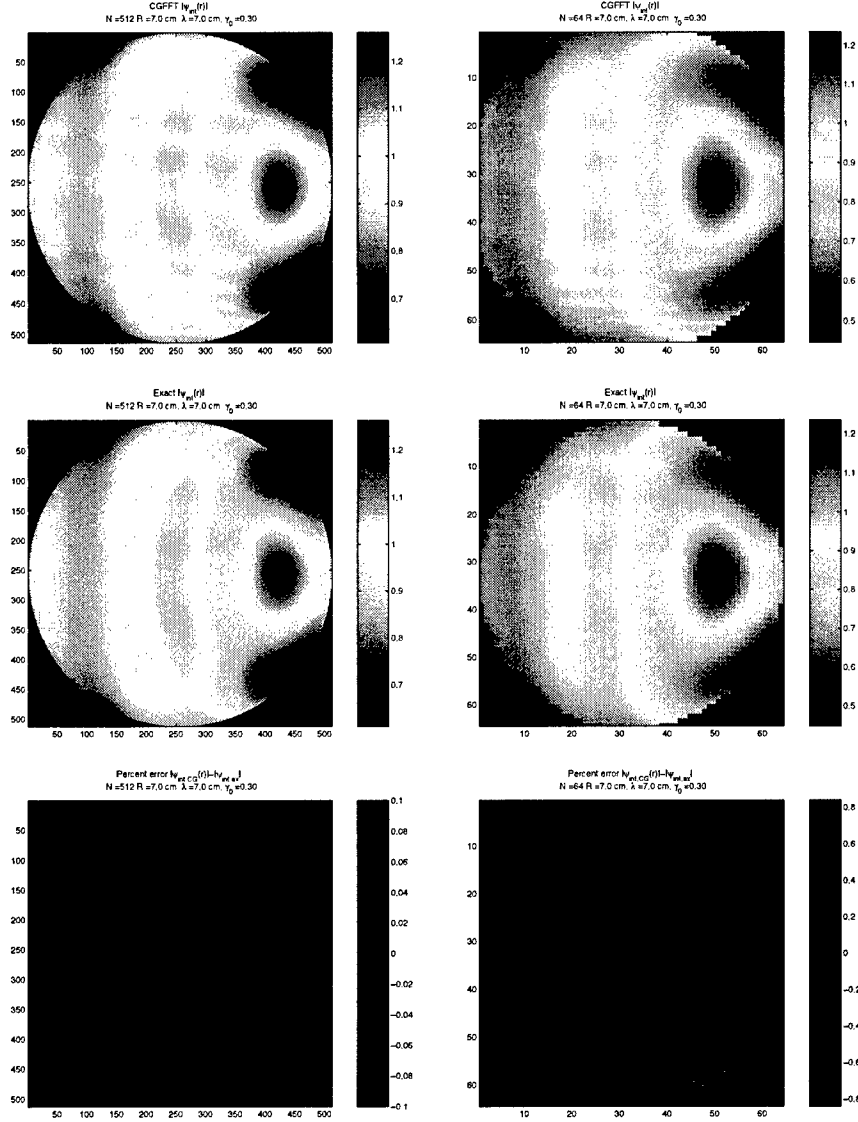


Figure 7: Comparison of  $\psi_{int}$  for CGFFT and the exact solution for scattering from an infinite cylinder, represented on a  $512 \times 512$  grid in the left panels and from a sphere, represented on a  $64 \times 64 \times 64$  grid in the right panels. The upper panels plot  $|\psi_{int}|$  from the CGFFT calculations, the middle plot  $|\psi_{int}|$  for the exact solution, and the bottom panels plot the relative error,  $(|\psi_{int,CG}| - |\psi_{int,ex}|)/|\psi_{int,ex}|$ . In both cases, the forward model was run with  $L = 14$  cm,  $\lambda = 7$  cm, and  $\gamma = 0.3$ .

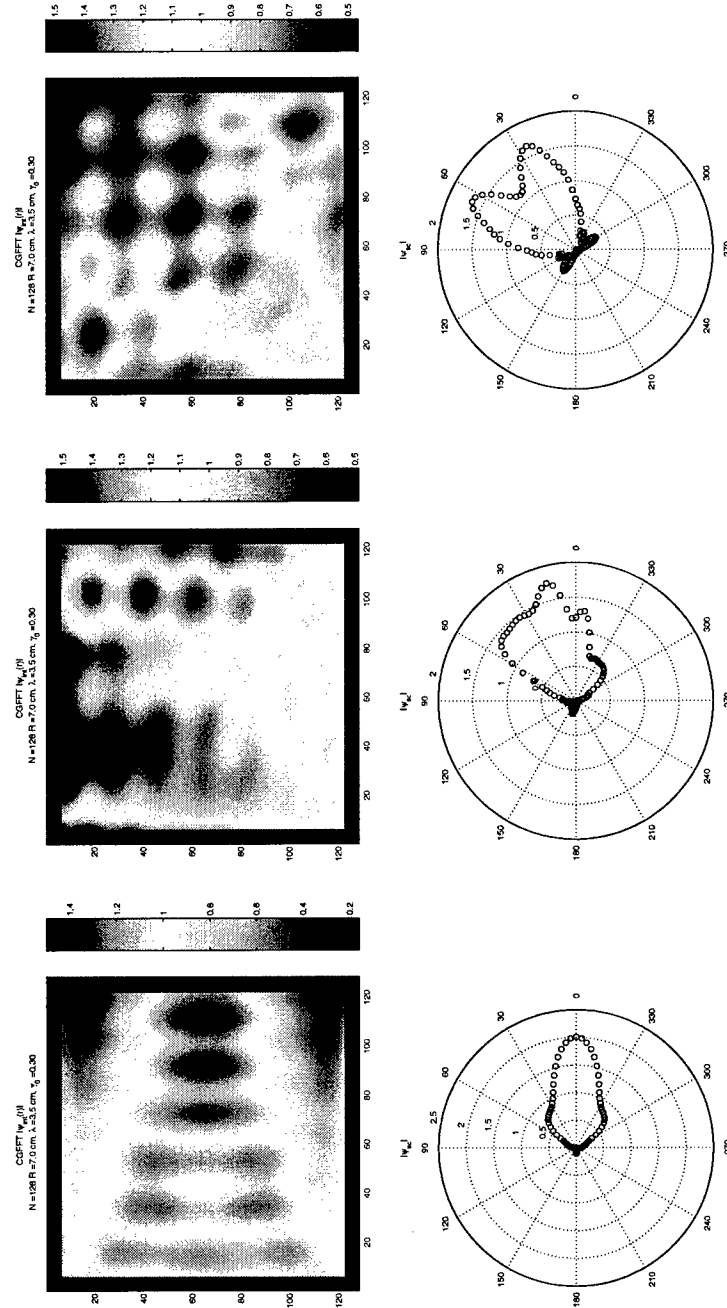


Figure 8: Internal (upper panels) and scattered field (lower panels) amplitudes computed for a  $128 \times 128$  square object with  $\gamma = 0.3$  and  $\lambda/L = 1/2$  for three plane waves having incidence angles of  $0$ ,  $\pi/8$ , and  $\pi/4$ .

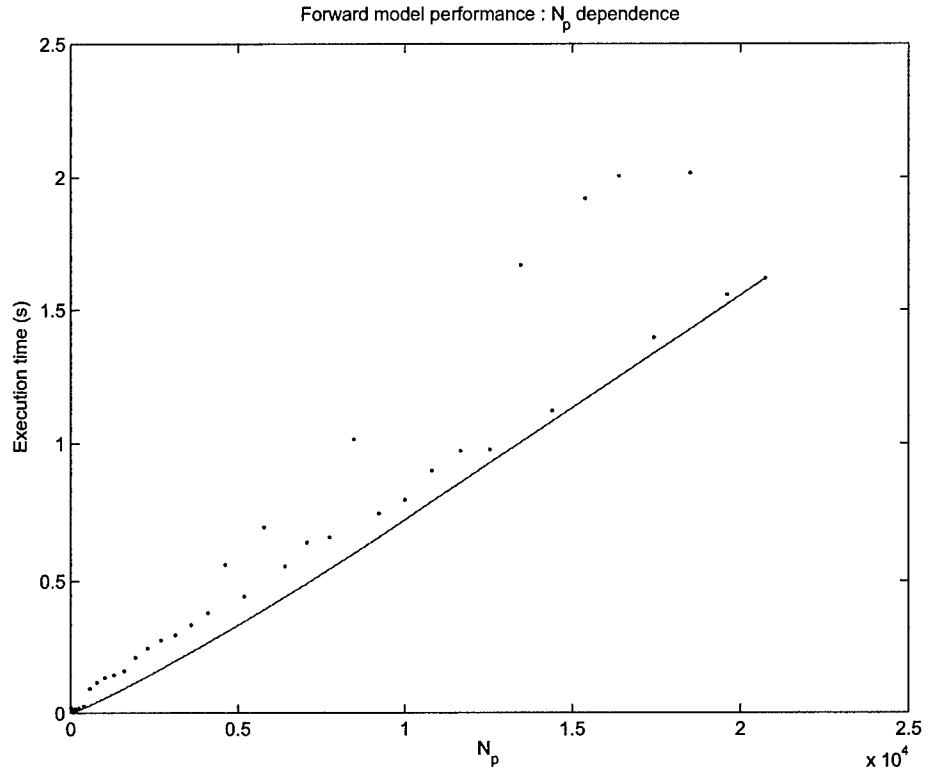


Figure 9: Scaling of forward model execution time with number of gridpoints in the scattering object. While some expected deviation is seen for smaller sizes, the overall trend can be seen to be dominated by the  $N_p \log N_p$  contribution from the FFT. Furthermore, the outlier points occur for FFT lengths whose greatest prime factor is  $\mathcal{F} \in \{13, 17, 19, 23, 29, 31\}$ , leading to well-known inefficiencies in FFT implementations, and for an FFT length of 128, which presumably causes cache collisions in the 2D case presented here.



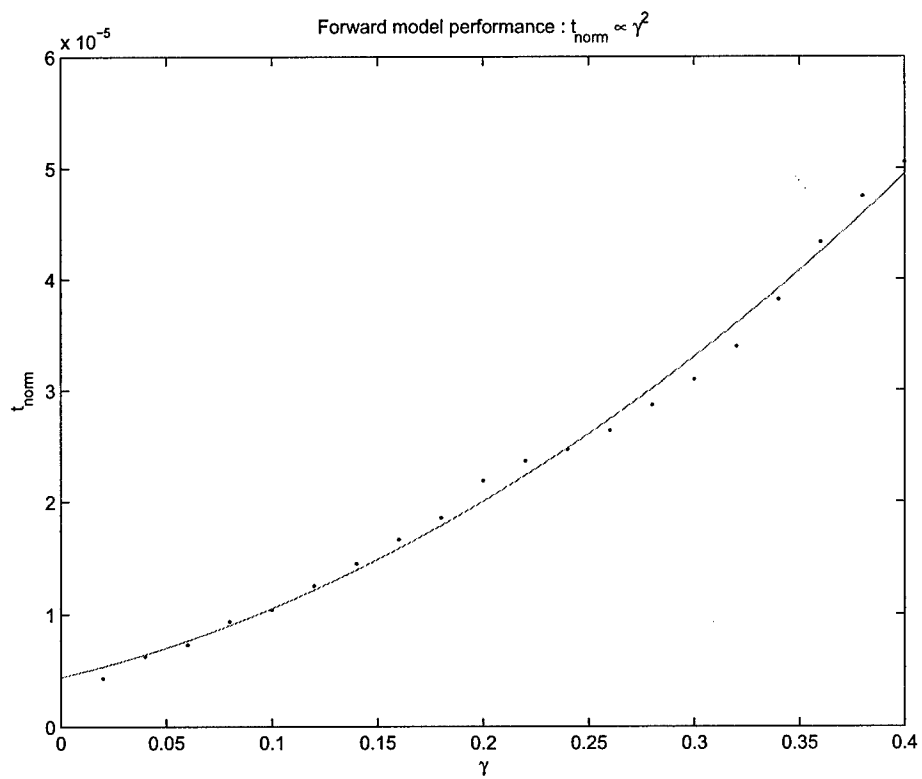


Figure 10: Scaling of normalized forward model execution time,  $t_{\text{norm}} = t_{\text{ex}}/N_p \log N_p$ , with  $\gamma$ , demonstrating a quadratic dependence of algorithm convergence with increasing deviation from Born-regime scattering.

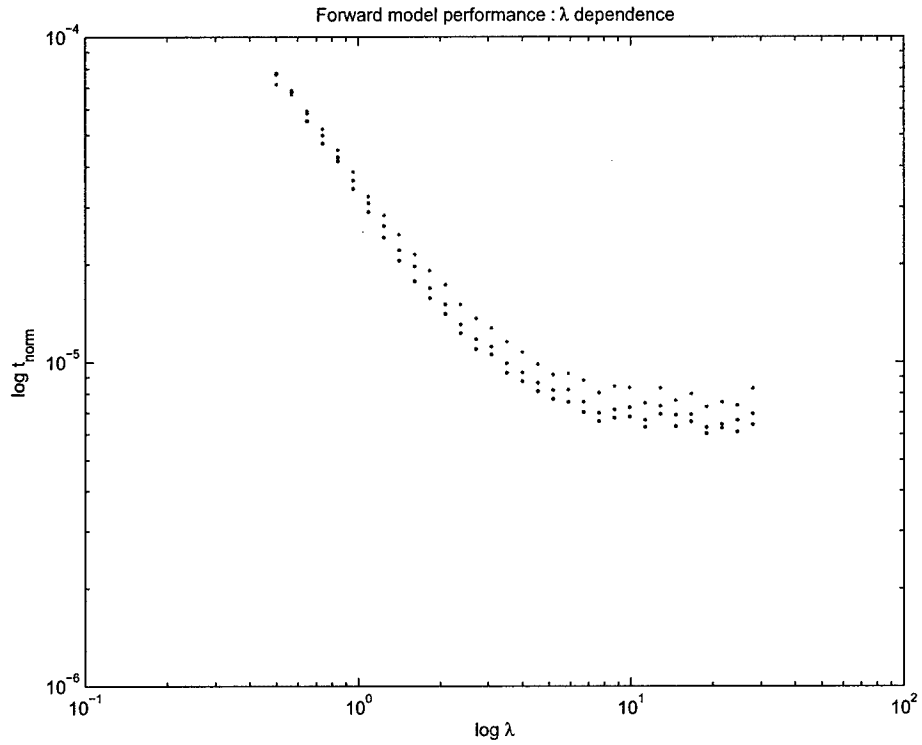


Figure 11: Scaling of normalized forward model execution time,  $t_{\text{norm}} = t_{\text{ex}}/N_p \log N_p$ , with  $\lambda$  for three values of  $N$  :  $\{64, 80, 96\}$ . Execution time is shown to obey a power law behavior, independent of  $N_p$ . Regression to the linear portion of the curves leads to a power-law relation of the form  $t_{\text{norm}} \propto 1/\lambda^{1.2}$ .